Journal of Experimental Botany, Vol. 75, No. 12 pp. 3731–3747, 2024
https://doi.org/10.1093/jxb/erae195 Advance Access Publication 27 April 2024

RESEARCH PAPER

Disrupting cell wall integrity impacts endomembrane trafficking to promote secretion over endocytic trafficking

Natalie Hoffmann, Eskandar Mohammad, and Heather E. McFarlane*

Department of Cell & Systems Biology, University of Toronto, M5S 3B2 Canada

* Correspondence: h.mcfarlane@utoronto.ca

Received 18 January 2024; Editorial decision 25 April 2024; Accepted 25 April 2024

Editor: Mads Eggert Nielsen, University of Copenhagen, Denmark

Abstract

The plant cell wall provides a strong yet flexible barrier to protect cells from the external environment. Modifications of the cell wall, either during development or under stress conditions, can induce cell wall integrity responses and ultimately lead to alterations in gene expression, hormone production, and cell wall composition. These changes in cell wall composition presumably require remodelling of the secretory pathway to facilitate synthesis and secretion of cell wall components and cell wall synthesis/remodelling enzymes from the Golgi apparatus. Here, we used a combination of live-cell confocal imaging and transmission electron microscopy to examine the short-term and constitutive impact of isoxaben, which reduces cellulose biosynthesis, and Driselase, a cocktail of cell-wall-degrading fungal enzymes, on cellular processes during cell wall integrity responses in Arabidopsis. We show that both treatments altered organelle morphology and triggered rebalancing of the secretory pathway to promote secretion while reducing endocytic trafficking. The actin cytoskeleton was less dynamic following cell wall modification, and organelle movement was reduced. These results demonstrate active remodelling of the endomembrane system and actin cytoskeleton following changes to the cell wall.

Keywords: Actin cytoskeleton, cell wall integrity, endocytosis, endosome, Golgi apparatus, isoxaben, plant cell walls, secretion, trafficking, *trans*-Golgi network.

Introduction

Plant cells are surrounded by a polysaccharide-rich cell wall that provides mechanical support, enables cell expansion, and acts as a physical barrier against biotic and abiotic stresses (Anderson and Kieber, 2020). Cell wall biosynthesis is mediated by the endomembrane system, which consists of the endoplasmic reticulum, Golgi bodies, the *trans*-Golgi network (TGN)/early endosomes, multi-vesicular bodies/pre-vacuolar compartments/late endosomes (LEs), the vacuole, and transport vesicles (Hoffmann *et al.*, 2021). The major structural component of the cell wall, cellulose, is produced by CELLULOSE SYNTHASE (CESA) enzymes that are trafficked through the Golgi and TGN before localizing to the plasma membrane where they are active (Pedersen *et al.*, 2023). The cell wall matrix polysaccharides, hemicelluloses and pectins, are synthesized by Golgi-resident proteins and then trafficked through the TGN prior to secretion to the cell wall (Hoffmann *et al.*, 2021). Vesicle

Abbreviations: CESA, CELLULOSE SYNTHASE; Dri, Driselase; FRAP, fluorescence recovery after photobleaching; GA-TGN, Golgi-associated *trans*-Golgi network; GI-TGN, Golgi-independent *trans*-Golgi network; ISX, isoxaben; LE, late endosome; LatB, LatrunculinB; PI, propidium iodide; TEM, transmission electron microscopy; TGN, *trans*-Golgi network.

trafficking and organelle movement are primarily dependent on a dynamic actin cytoskeleton, associated myosin motors, and actin–myosin-driven cytoplasmic streaming (Nebenführ *et al.*, 1999; Sampathkumar *et al.*, 2013).

The structure and composition of the cell wall is not static and responds both to developmental cues and to external stress. Recent research has uncovered the existence of a complex cell wall integrity mechanism in which changes to cell wall structure activate intracellular signalling that can act to correct or alleviate cell wall modifications (Vaahtera *et al.*, 2019). This sensing system is intricately linked with the mechanical strength of the cell wall and turgor pressure, as these forces work against each other to prevent cell bursting (Bacete and Hamann, 2020). Other known stimulators of cell wall integrity signalling include low molecular mass cell wall fragments, such as pectin-derived oligogalacturonides (Voxeur *et al.*, 2019) or cellulose-derived compounds (Tseng *et al.*, 2022; Martín-Dacal *et al.*, 2023). Recent work has identified several receptors that are involved in perceiving cell wall modification and the immediate downstream processes following activation. These include post-translational modifications (Wang *et al.*, 2020; Tseng *et al.*, 2022), alterations to gene expression, increased salicylic acid and jasmonic acid phytohormones, and production of reactive oxygen species (Hamann *et al.*, 2009; Wormit *et al.*, 2012; Engelsdorf *et al.*, 2018; Gigli-Bisceglia *et al.* 2018; Chaudhary *et al.*, 2020; Bacete *et al.*, 2022). Cell wall composition also changes in response to cell wall integrity signalling. For example, cell wall changes have been documented following pathogen infection (Chowdhury *et al.*, 2014) or reduced cellulose biosynthesis (Hamann *et al.*, 2009), including deposition of callose or the phenolic polymer lignin (Denness *et al.*, 2011; Chaudhary *et al.*, 2020). Furthermore, inhibition of cellulose biosynthesis led to up-regulation of genes involved in cell wall remodelling (Duval and Beaudoin, 2009; Hamann *et al.*, 2009). Although CESA secretion to the plasma membrane is altered during cell wall integrity responses (McFarlane *et al.*, 2021), it is unclear whether matrix polysaccharide and cell wall protein secretion are also altered by activation of cell wall integrity signalling. Therefore, the specifics of how endomembrane system organization and function change in response to cell wall disruption, as well as the underlying mechanisms for these changes, are still unknown.

Increasing evidence supports the role of the TGN/early endosomes in mediating responses during developmental and stress conditions (Uemura *et al.*, 2019; Oda *et al.*, 2020). High resolution imaging has shown that within a single TGN there are distinct subdomains mediating secretory, endocytic, and vacuolar trafficking pathways (Heinze *et al.*, 2020; Shimizu *et al.*, 2021). Imaging techniques have also identified two populations of TGN: Golgi-associated TGN (GA-TGN) and Golgi-independent TGN (GI-TGN) (Viotti *et al.*, 2010; Kang *et al.*, 2011; Uemura *et al.*, 2014, 2019). GA-TGN and GI-TGN are thought to represent functionally distinct compartments, with GA-TGN being involved in both endocytic and secretory pathways and GI-TGN being primarily involved in secretion (Kang *et al.*, 2011; Uemura *et al.*, 2019). The proportion of GI-TGNs increased during root development (Uemura *et al.*, 2014) and following powdery mildew infection (Uemura *et al.*, 2019), suggesting that increasing the number of GI-TGNs could promote secretory trafficking under specific conditions.

In this study, we characterized how endomembrane system structure and function respond to cell wall modifications induced by isoxaben (ISX) treatment, which inhibits cellulose biosynthesis (Scheible *et al.*, 2001), or following damage to the cell wall using Driselase (Dri), which contains a combination of fungal cell wall-degrading enzymes, including cellulase, xylanase, mannanase, and pectinase (Kubicek *et al.*, 2014; Engelsdorf *et al.*, 2018). Using live-cell confocal imaging and high-resolution electron microscopy, we show that ISX or Dri treatment imparts distinctive effects on the endomembrane system under short-term and constitutive treatments. Both conditions reduced the dynamics of the actin cytoskeleton and adjusted the balance between endocytic trafficking and secretion to favour increased secretion, presumably to accommodate increased trafficking from the Golgi apparatus to fortify the cell wall.

Materials and methods

Plant materials

The Arabidopsis Columbia-0 (Col-0) accession was used in this study. Fluorescent lines used for this study are listed in Supplementary Table S1.

Growth conditions

Seeds were surface-sterilized for 10 min using 3% sodium hypochlorite (Javel) and 0.1% Triton X-100 (Thermo Fisher Scientific) and rinsed five times in sterile water, then sown on half strength Murashige and Skoog (½ MS) medium with vitamins (Phyto Technology Laboratories) with 2.5 mM MES (Thermo Fisher Scientific) and 0.7% agar (Thermo Fisher Scientific) at pH 5.8, supplemented with 1% w/v sucrose (Thermo Fisher Scientific). Seeds were then stratified for 2–4 d at 4 °C. For root analyses, seedlings were grown vertically for 5 d under ~100 µmol m^{-2} s^{-1} light at 21 °C for 18 h and in the dark at 18 °C for 6 h. For etiolated hypocotyl analyses, seeds were light-treated for 5 h and then grown in the dark for 5 d under the same temperature cycle.

Stress and inhibitor treatments

Either 20 mM or 20 µM stock solutions of isoxaben (ISX; Sigma-Aldrich, cat. no. 36138) were prepared in 100% ethanol and stored at −20 °C. ISX was added to slightly cooled molten ½ MS + sucrose + agar before being poured into plates with a final concentration of no more than 0.001% v/v ethanol in the medium. A 2% w/v solution of Driselase (Dri; Sigma-Aldrich, cat. no. D9515) was prepared in deionized H_2O and filter-sterilized, then added to slightly cooled molten ½ MS + sucrose + agar before being poured into plates. To ensure Dri enzyme activity, plates were made fresh for each experiment and used for no longer than 1 week.

For constitutive treatment, seeds were directly germinated on stress medium (½ MS + sucrose + 2 nM ISX or 0.03% Dri) and grown for 5 d. For short-term treatments, seeds were germinated on sterile filter-paper strips on ½ MS + 1% sucrose plates and grown for 5 d. The filter-paper

strips were gently transferred to stress medium plates (+200 nM ISX or +0.05% Dri) and left to grow vertically in the growth chamber for the designated times. As a control, seeds were mock-treated for 4 h with an equal volume of ethanol for a final concentration of 0.001% v/v.

For boiled Dri control experiments, 0.03% or 0.05% Dri solution was heat-inactivated at 100 °C for 10 min, prior to being added to ½ MS + 1% sucrose medium. Boiled Dri plates were then used for root growth assays and for root morphology imaging, and were compared with no treatment (NT) plates (½ MS + sucrose).

A 10 mM stock of LatrunculinB (LatB) from *Latruncula magnifica* (Sigma-Aldrich, cat. no. L5288) was prepared in dimethyl sulfoxide (DMSO) and stored at −20 °C. For short-term treatments, a 25 μM working solution was prepared in liquid ½ MS + 1% sucrose. For fABD2–green fluorescent protein (GFP) imaging and NAG–GFP speed quantification, 5-day-old seedlings were treated with LatB for 1 h prior to imaging. For co-treatment of LatB with either ISX or Dri, 5-day-old seedlings were incubated in liquid ½ MS + 1% sucrose with 0.25% DMSO (Mock), 25 μM LatB, 200 nM ISX, or 0.05% Dri for 4 h or 24 h prior to measuring root length.

Quantification of seedling phenotypes

For seedling growth assays, plates of 5-day-old seedlings were scanned using an Epson V550 photo scanner. Quantification of root or etiolated hypocotyl lengths was performed manually in FIJI (Schindelin *et al.*, 2012). For calculation of the change in length following short-term stress treatments, the length of each stress-treated seedling was divided by the mean length of mock-treated seedlings at a given time point. Data were consistent for at least three independent experiments.

Fluorescent dyes

A 0.5 mg ml^{-1} stock solution of propidium iodide (PI; Thermo Fisher Scientific, cat. no. AC440300250) was prepared in deionized H_2O and stored at 4 °C in the dark. Five-day-old seedlings were incubated in a 15 μM working solution in deionized H_2O for 15 min in the dark prior to being imaged.

Molecular Probes FM1-43 (Thermo Fisher Scientific, cat. no. T35356) was suspended in DMSO to 15 μM and stored at −20 °C in the dark. For FM1-43 uptake quantification, 5-day-old roots were incubated in a 1.5 μM solution in liquid ½ MS + 1% sucrose for 5 min on ice, rinsed in ½ MS twice on ice, then mounted on a slide (denoting start of endocytosis). Epidermal cells in the elongation zone were monitored for 30 min, taking an image every 1 min. In a separate experiment, roots were stained with FM1-43 and rinsed as above, then cells in the elongation zone were imaged following 60 min of FM1-43 uptake.

Confocal microscopy

Seedlings were mounted on a custom-built slide (Verbančič *et al.*, 2021) in water under a pad of 0.8% agarose. For root analyses, all imaging was performed on the early elongation zone of roots. Seedlings were imaged using a Nikon Eclipse Ti2-E inverted microscope equipped with a CSU-W1 spinning disk with dual Photometrics Prime95b sCMOS cameras. Fluorophores were excited using a 488 nm laser for GFP (90 mW, 0.5% power for NAG–GFP co-localization analyses and 19% power for all other imaging) and a 561 nm laser for red fluorescent protein (RFP; 70 mW, 60% power for VHAa1–RFP co-localization analyses and 24% for all other imaging). Fluorescence emission was collected using a band emission filter of 525/36 nm for GFP and 605/52 nm for RFP. For analysis of dual fluorescent lines, the 488 nm and 561 nm lasers were excited simultaneously and emission was separated with a 561 nm long-pass dichroic mirror. For FM1-43 or PI staining, the dye was excited using the 488 nm or 514 nm (30 mW, ~25% power) laser, respectively, and collected using the 605/52 nm emission filter. All images were collected using either a ×40 oil-immersion objective lens (CFI Plan Fluor, NA 1.3, WD 0.24) or a ×100 oil-immersion objective lens (Apochromat TIRF, MRD01991, NA 1.49, WD 0.12). Pixel size for the ×100 objective lens is 110 nm (9.0909 pixels μm^{-1}). Laser settings and exposure times were kept identical between treatments and biological replicates of the same experiment.

Quantification of cell perimeter, volume, and cell death

Images of the elongation zone of PI-stained roots taken with the ×40 objective were used to calculate the size and volume of cells following ISX and Dri treatment. *z*-Stacks of depth 4–21 μm were isolated for individual cells that had started elongating but prior to formation of root hairs (i.e. the maturation zone). Due to differences in root growth between treatments, the length of this zone differed between treatments, but the zone was evident due to the presence of swollen cells for ISX treatment. Cell perimeter (for a rectangular cell, or circumference for swollen ISX cells) was calculated manually from maximum projection images in FIJI. $n>16$ cells from four to eight biological replicates per treatment. Due to difficulties in approximating the volume of bulging cells and swollen cells for ISX-treated roots using standard mathematical equations for cuboids or perfect spheres, cell volume was calculated manually from these images by measuring the surface area and known *z*-step height for each image within a *z*-stack; $n>16$ cells from four to eight biological replicates per treatment.

The number of dead cells per root was counted manually by identification of PI-stained nuclei in ×40 images. Cells only within the elongation zone of roots were assessed, starting after the root apical meristem where cells are starting to elongate (and start to swell for ISX/Dri treatment) and ending prior to formation of root hairs. PI is normally excluded from internal staining of intact living cells, but if the cell is non-viable PI will enter the cell and bind to DNA. $n>4$ roots per treatment.

Fluorescence recovery after photobleaching

Fluorescence recovery after photobleaching (FRAP) of PIP2A–GFP or LTI6B–GFP was performed on 5-day-old roots using the ×100 objective. A circular region of interest (12 μm diameter) at the plasma membrane was completely bleached using the 405 nm laser (50 mW) at 100% intensity with a 100 μs dwell. For PIP2A–GFP, fluorescence recovery was monitored for 30 min, with an image taken every 2 min. For LTI6B–GFP, fluorescence recovery was monitored for 5 min, with an image taken every 2.5 s. Quantification was performed as per McKenna (2022), using data normalized to pre-bleach values.

Quantification of endocytosis and endocytic trafficking using FM1-43

The plasma membrane signal for any given time point was calculated by manually outlining single cells, and subtracting the fluorescence intensity of the cytoplasm from the fluorescence intensity of the whole cell (denoting plasma membrane signal) using measurements from FIJI (Schindelin *et al.*, 2012). Data are representative of n=17–24 cells from each time point from six biological replicates.

Quantification of organelle size

Five-day-old roots were imaged using the ×100 objective. Regions of interest from NAG–GFP/VHAa1–mRFP or WAVE7–RFP were selected from *z*-stacks (100 pixels×100 pixels with 0.2 μm *z*-spacing, for a total of 4 μm stack). Regions of interest were manually thresholded in FIJI, with a minimum object size of 50 pixels and a maximum object size of 1000 pixels for NAG–GFP and WAVE7–RFP, and a minimum object size of

10 pixels and a maximum object size of 1000 pixels for VHAa1–mRFP. The size of organelles was calculated using the 'AnalyzeParticles' plugin. n=34 regions of interest for Golgi/TGN and n=24 for late endosomes from 12–15 biological replicates.

Quantification of organelle number and co-localization using DiAna

Regions of interest from NAG–GFP/VHAa1–mRFP or WAVE7–RFP were selected from z-stacks (100 pixels×100 pixels with 0.2 µm z-spacing, for a total of 4 µm stack) and segmented using the DiAna plugin on FIJI (Gilles *et al.*, 2017). Regions of interest were manually thresholded, with a minimum object size of 50 pixels and a maximum object size of 1000 pixels for NAG–GFP, and a minimum object size of 10 pixels and a maximum object size of 1000 pixels for VHAa1–mRFP. Segmented objects were used to calculate organelle number, distance between organelles, and co-localization using default settings. n=34 regions of interest from 12 biological replicates.

The number of GA- and GI-TGNs was calculated using NAG–GFP/VHAa1–mRFP regions of interest. GA-TGNs were identified as TGNs significantly co-localizing with a Golgi body whereas GI-TGNs were identified as TGNs not significantly co-localizing with a Golgi body, using a segmented 3D image in DiAna. GI-TGNs were manually confirmed on the image, with GI-TGNs being VHAa1–mRFP TGN that are physically separate from a NAG–GFP Golgi body and move independently (Uemura *et al.*, 2014).

Quantification of organelle speed

Five-day-old NAG–GFP or WAVE7–RFP roots were used to monitor organelle speed using the ×100 objective. A 1.2 µm (0.2 µm z-spacing) z-stack was imaged every 2 s for a total time of 30 s. A 100 × 100 pixel region of interest for each time point was generated in FIJI (Schindelin *et al.*, 2012), and individual organelle speeds were calculated manually using the 'ManualTracking' plugin using default parameters. n>78 Golgi per treatment from six biological replicates for NAG–GFP, and n>126 late endosomes for WAVE7-RFP from six biological replicates.

For washout experiments, 5-day-old roots were treated with 200 nM ISX or 0.05% Dri for 24 h, then transferred to ½MS + 1% sucrose medium (without ISX or Dri) for 2 h prior to imaging.

Quantification of actin occupancy and dynamics

Actin occupancy (measure of local abundance) was measured based on Higaki (2017). Briefly, z-stacks of fABD2–GFP roots (depth 5–6 µm, spacing 0.5 µm) were taken with a ×100 objective. In FIJI, z-stacks were converted into maximum projections and cropped into 100 × 100 pixel regions of interest, with each region representing one cell or region of a cell. Maximum projections were manually thresholded to remove background, smoothed, and skeletonized using the Skeleton 2D/3D plugin. The density of the skeletonized actin cytoskeleton was measured and compared with the area of the region to obtain actin density. n>25 regions of interest per treatment from eight biological replicates.

For actin dynamics, 5-day-old fABD2–GFP roots were imaged using the ×100 objective lens. A 5–6 µm z-stack (0.5 µm per step) was imaged every 2 s for a total time of 2 min. A 100 × 100 pixel region of interest for each time point was generated in FIJI (Schindelin *et al.*, 2012), and the maximum projection images were used for analysis. The FIJI macro JaCoP (Bolte and Cordelières, 2006) was used to calculate Pearson's correlation coefficient between sequential time points (time point 1 versus time point 2, time point 2 versus time point 3, etc.). Three regions of interest per image were averaged for one replicate. A high Pearson's correlation coefficient indicates low dynamics (actin does not change frame-to-frame) whereas a low correlation coefficient indicates high dynamics (actin organization does not stay the same frame-to-frame). n>25 regions of interest per treatment from eight biological replicates.

Ratiometric sec–GFP quantification

Five-day-old ratiometric sec–GFP roots were used to monitor secretion using the ×100 objective. A 2 µm z-stack (0.2 µm spacing) of GFP and RFP was imaged. A 50 × 50 pixel region of interest was generated in FIJI (Schindelin *et al.*, 2012). Using the maximum projection image, the fluorescence intensities of GFP and RFP channels were measured and compared. n=36 regions of interest from six biological replicates per treatment.

Transmission electron microscopy cryofixation and embedding

Five-day-old root tips were dissected and submerged in 1-hexadecene (Sigma-Aldrich, cat. no. H2131) as a cryoprotectant prior to loading into B-type high-pressure freezing planchets (Electron Microscopy Sciences, cat. no. 71167). Samples were frozen with a high-pressure freezer (Leica EM ICE) and transferred to freeze-substitution vials under liquid nitrogen. Samples were freeze-substituted in 8% (v/v) 2,2-dimethoxypropane (Sigma-Aldrich, cat. no. D136808) and 2% (w/v) osmium tetroxide (Electron Microscopy Sciences, cat. no. 19100) in anhydrous acetone over 5 d at −85 °C, slowly brought to room temperature over 3–4 h, separated from their sample carrier, and rinsed with anhydrous acetone five times. Spurr's resin (Electron Microscopy Sciences, cat. no. 14300) was gradually infiltrated in an ascending series of 10, 20, 30, 40, 50, 60, 80, and 100% resin for 2–3 h each or overnight. Two additional 100% resin exchanges were performed for 3 h each, and then samples were polymerized in BEEM embedding capsules (Electron Microscopy Sciences) for 24 h at 65 °C.

Transmission electron microscopy sectioning and imaging

Sections of ~70 nm were cut with a DiATOME knife on a Leica Ultracut E ultramicrotome, suspended on copper grids (ProSci Tech) coated with 1% formvar (Electron Microscopy Sciences). Samples were poststained with UranyLess (Electron Microscopy Sciences, cat. no. 22409) for 1 min and Reynolds' lead citrate (Reynolds, 1963; all chemicals from Thermo Fisher Scientific) for 10 min. Grids were imaged using a Hitachi HT7700 transmission electron microscope at 80 kV accelerating voltage with a tungsten filament coupled to an AMT XR-111 digital camera. Images were captured with AMT Capture Engine software.

Transmission electron microscopy quantification

Quantification of Golgi ultrastructure was performed manually using FIJI; see Supplementary Fig. S8 for a description of parameters.

Data visualization

Most data (n>24) are presented in a violin plot, which is a kernel density plot that ranges from the minimum to the maximum value. Within each violin plot there is a box plot. The box represents the 25–75% quartiles, and the median is represented by a horizontal line within the box. The whiskers of the box represent the minimal and maximal values of the sample.

Results

Changes in cell wall integrity induced by isoxaben or Driselase impact plant growth and cell morphology

To test the impact of cell wall integrity responses on cellular processes, we utilized two commonly used treatments,

isoxaben (ISX), which inhibits cellulose biosynthesis (Scheible *et al.*, 2001), and Driselase (Dri), a cocktail of fungal enzymes including cellulases, xylanases, mannanases, and pectinases (Engelsdorf *et al.*, 2018). Cellular and molecular responses to ISX have been extensively documented in a time-dependent manner (Supplementary Fig. S1A). However, many of these studies used a high concentration of ISX (600 nM), which under our conditions induced substantial cell death in the root elongation zone after 4 h as indicated by PI staining of the nucleus (Supplementary Fig. S1B). We therefore tested a range of concentrations and durations for both ISX and Dri to assess the impact on seedling growth and cell morphology.

Wild-type Col-0 seedlings germinated and grown on ½ MS medium including 1% sucrose and a range of concentrations of ISX (0.5–5 nM) for 5 d showed a reduction in root and etiolated hypocotyl length and substantial cell swelling at higher concentrations (Supplementary Fig. S2). Short-term treatment with 200 nM ISX, which had lower amounts of cell death relative to 600 nM ISX (Supplementary Fig. S1C), caused initial cell swelling as early as 4 h, and reduced root length was apparent after 24 h (Supplementary Fig. S3). Consistent with previous work (Gutierrez *et al.*, 2009), imaging of fluorescently tagged CELLULOSE SYNTHASE3 (GFP–CESA3) (Desprez *et al.*, 2007; Crowell *et al.*, 2009) in root cells showed decreased GFP–CESA3 abundance at the plasma membrane after 1 h of 200 nM ISX (Supplementary Fig. S3E), confirming ISX is active and sufficient to trigger CESA internalization and reduce cellulose synthesis. From these results, we selected a short-term treatment of 200 nM ISX for 4 h and 24 h and a constitutive 5 d treatment on 2 nM ISX, which represent initial cell swelling, the onset of root growth inhibition/severe cell morphological changes, and a constitutive treatment, respectively, to assess the impact of ISX on cellular processes.

The effect of Dri on wild-type Col-0 showed differing effects relative to Mock, compared with ISX treatment. Constitutive growth on ½ MS medium with 1% sucrose and a range of concentrations of Dri showed reduced root length and degradation of the root apical meristem, but comparably minor changes in etiolated hypocotyl length or morphology (Supplementary Fig. S4). Short-term treatments with 0.05% Dri decreased root length after 4 h, with initial cell swelling observed at this time (Supplementary Fig. S5). We therefore selected a short-term treatment of 0.05% Dri for 4 h and 24 h and a constitutive 5 d treatment on 0.03% Dri. Due to the comparably minor effect of Dri on etiolated hypocotyls, we focused subsequent work on the elongation zone of light-grown roots, which is highly sensitive to stress treatments (Hamann *et al.*, 2009). Treatment with boiled Dri eliminated the degradation of the root apical meristem at all time points and did not cause root growth inhibition at 4 h, but still caused some cell swelling and root growth inhibition after 24 h and 5 d treatment (Supplementary Fig. S6A, B), suggesting that non-enzymatic components of Dri also somewhat impact root growth and morphology.

Following selection of the ISX and Dri concentrations and time points, we performed further morphological analysis using the PI-stained roots of both ISX and Dri treatments. Cell size and volume increased significantly following 24 h ISX treatment due to cell swelling (Supplementary Fig. S6C, D). We also used internal staining of nuclei with PI as a proxy for cell death, and found that 4 h and 24 h ISX had significantly more cell death relative to Mock-treated controls, consistent with previous work (Hamann *et al.*, 2009), and there was also increased cell death following 5 d Dri treatment (Supplementary Fig. S6E). Despite the increased cell death, the vast majority of cells at the lower (200 nM) ISX concentration were still viable, as were the cells in the Dri-treated roots under our growth conditions. Together, the combination of short-term and constitutive treatments allowed us to specifically dissect early, middle-term, and long-term responses to cell wall modification induced by ISX or Dri (Fig. 1).

Disrupting cell wall integrity increases secretion to the cell wall

Cell wall fortification under cell wall integrity stress requires secretion from the Golgi apparatus and TGN: matrix polysaccharides are synthesized at the Golgi apparatus and secreted to the cell wall (Hoffmann *et al.*, 2021) and CESAs are trafficked through the Golgi apparatus to synthesize cellulose at the plasma membrane (Zhu and McFarlane, 2022). Therefore, we assessed the impact of ISX and Dri treatment on Golgi and TGN morphology using the dual fluorescent marker line NAG–GFP/VHAa1–mRFP (Fig. 2A; Supplementary Fig. S7A, B), which labels *cis*-Golgi cisterna via an *N*-acetylglucosaminyltransferase, which is part of the *N*-glycosylation pathway (NAG–GFP), and the TGN with VHAa1, a component of the V-type H^+-ATPase that maintains the pH of the TGN (Grebe *et al.*, 2003; Dettmer *et al.*, 2006), in root elongation zone epidermal cells. Golgi body size significantly increased following 24 h ISX and both 4 h and 24 h Dri treatments (Fig. 2B), but there were no changes to Golgi body number (Fig. 2C). There were also no significant differences for VHAa1–mRFP-labelled TGN size (Fig. 2D) or number (Supplementary Fig. S7C). Use of the dual Golgi and TGN marker allowed us to dissect whether a TGN was Golgi-associated (GA-TGN) or Golgi-independent (GI-TGN), based on co-localization with a Golgi body and movement together with, or independently of, a Golgi stack (Uemura *et al.*, 2014). Association between Golgi and TGN was higher in 24 h ISX treatment, as there was a significantly lower distance between the two organelles (Supplementary Fig. S7D). The proportion of GI-TGNs in Mock-treated roots was similar to those observed by Uemura *et al.* (2019). ISX or Dri treatment did not significantly alter the number of GA-TGNs or GI-TGNs (Supplementary Fig. S7E, F), resulting in a similar GI-TGN:GA-TGN proportion between treatments (Fig. 2E). These results suggest that Golgi body size increases following short-term ISX or Dri, but there are no changes to the size or number of TGNs.

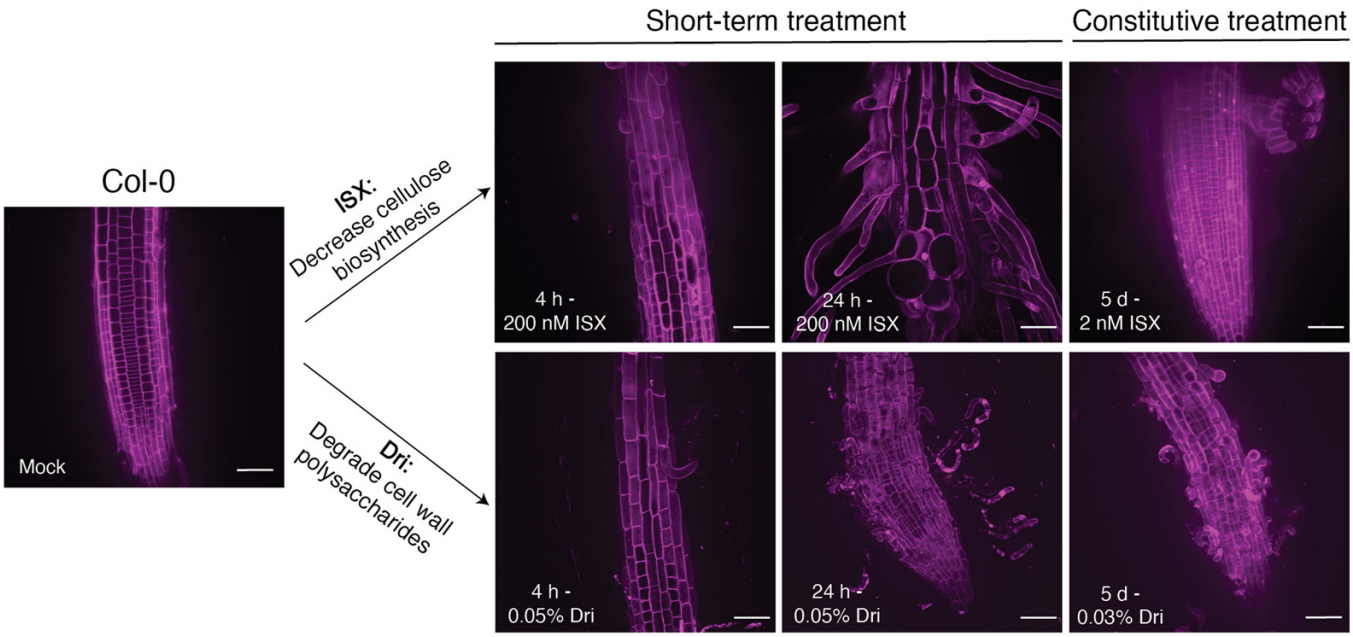

Fig. 1. Summary of the treatments used in this work. Arabidopsis Col-0 was treated with either isoxaben (ISX), which reduces cellulose biosynthesis, or Driselase (Dri), a combination of fungal enzymes that degrades cellulose, hemicelluloses, and pectins. For short-term treatments, 5-day-old roots were transferred to medium containing either 200 nM ISX or 0.05% Dri and left to grow for 4 h or 24 h. For constitutive treatment, Col-0 seeds were germinated and grown on medium containing 2 nM ISX or 0.03% Dri for 5 d prior to analysis. Mock-treated Col-0 seedlings were treated with an equal volume ethanol for 4 h. Images are maximum-projection images of PI-stained root tissue and are representative of six biological replicates. Scale bars are 50 μm.

To examine further whether ISX or Dri treatment impacts the size or morphology of GA-TGN and GI-TGNs, we assessed Golgi body and TGN ultrastructure at high resolution using transmission electron microscopy (TEM) of high-pressure frozen, freeze-substituted roots. Due to the fragile state of 24 h-treated roots, we instead looked at early ultrastructural changes following 4 h of ISX or Dri treatment (Fig. 2F; Supplementary Fig. S8). Overall cell and cell wall morphology was similar between Mock and ISX treatments, while there was cell wall degradation and cell detachment observed during Dri treatment (Supplementary Fig. S8A–C). We next examined four parameters of Golgi and TGN ultrastructure, including the length of Golgi cisterna, the diameter of the margins of *trans*-Golgi cisternae (a measure of vesicle formation), and the diameter of TGN vesicles at both the GA-TGN and the GI-TGN (Supplementary Fig. S8G). There were no differences in Golgi ultrastructure between treatments (Supplementary Fig. S8H, I), but for Dri treatment, there was a significant increase in GA-TGN vesicle diameter (Fig. 2G). Together, these results suggest that Golgi and TGN number are unchanged following ISX or Dri treatment, but short-term treatment increases the size of Golgi bodies following either ISX or Dri, and increases the size of the GA-TGN following Dri treatment.

We next asked whether anterograde secretion to the plasma membrane and cell wall was impacted by ISX or Dri treatment. Since there are currently no methods to track polysaccharide secretion from the Golgi apparatus directly using live-cell imaging, we used a ratiometric secreted GFP (ratiosec–GFP) marker, in which a vacuolar-targeted RFP is produced in equimolar amounts to a secreted form of GFP (Samalova *et al.*, 2006), to quantify protein secretion of GFP to the apoplast (Supplementary Fig. S9). Short-term 4 h and 24 h treatments of ISX or Dri showed increased secretion of GFP, while constitutive treatments had only a minor effect. Since the accumulation of GFP in the apoplast is pH-sensitive, and cell wall integrity signalling can increase the pH of the apoplast (Kesten *et al.*, 2019), we decided to confirm these results by assessing the real-time secretion of the plasma membrane protein PIP2A–GFP, a putative aquaporin (Cutler *et al.*, 2000), using FRAP experiments (Fig. 3A; Supplementary Fig. S10). PIP2A–GFP was previously shown to be a good marker for *de novo* secretion, as it shows very limited diffusion in the plasma membrane (Luu *et al.*, 2012). Interestingly, both 4 h and 24 h ISX treatments showed a significant increase in fluorescence recovery 30 min after photobleaching, relative to Mock treatment, with 4 h Dri treatment also showing a significant increase in recovery (Fig. 3B, C).

While PIP2A–GFP exhibits low diffusion in the plasma membrane under standard conditions (Luu *et al.*, 2012), previous work showed that the lateral mobility of plasma membrane-localized proteins increased following separation of the plasma membrane from the cell wall via plasmolysis or cell wall degradation (Feraru *et al.*, 2011; Martinière *et al.*, 2012),

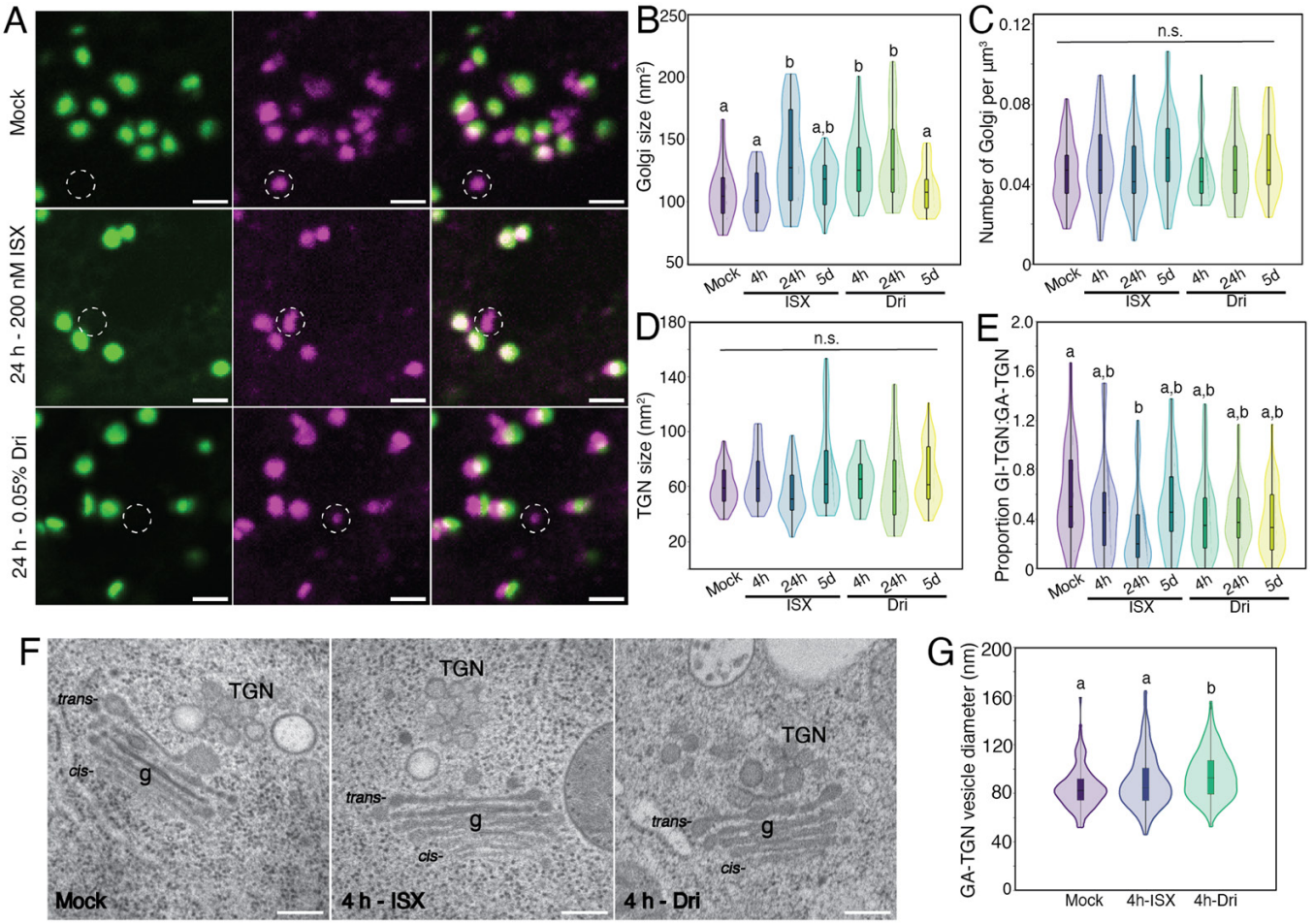

Fig. 2. Treatment with isoxaben (ISX) or Driselase (Dri) impacts Golgi and *trans*-Golgi network (TGN) morphology. (A) Representative maximum-projection images of 5-day-old Col-0 root elongation zone epidermal cells with the dual Golgi (green) and TGN (magenta) marker NAG–GFP/VHAa1–RFP. White dashed circles indicate Golgi-independent *trans*-Golgi network (GI-TGN). Scale bar is 2 µm. (B) Quantification of Golgi size. (C) Quantification of the number of Golgi bodies. (D) Quantification of TGN size. (E) Proportion of GI-TGN to Golgi-associated *trans*-Golgi network (GA-TGN). (F) Representative TEM images of Mock-, 4 h-ISX-, or 4 h-Dri-treated 5-day-old high-pressure frozen root elongation zone epidermal cells. Scale bars are 200 nm. g denotes Golgi bodies, *cis-*/*trans-* denotes the face of the Golgi. (G) Quantification of GA-TGN vesicle diameter. See Supplementary Fig. S8 for more information about TEM parameters. For fluorescence imaging, n=34 regions of interest from each treatment from 12 biological replicates. For TEM, n=83, 123, and 182 TGN from Mock, 4 h ISX, and 4 h Dri, respectively, from three biological replicates. Letters indicate significantly different means using a one-way ANOVA with a Dunn's post-hoc test with Bonferroni correction, P<0.05; n.s., not significant.

and ISX treatment decreased the total range of movement of proteins (Martinière *et al.*, 2012). We therefore performed FRAP experiments using LTI6B–GFP (Cutler *et al.*, 2000), a single-pass transmembrane protein that shows fast lateral diffusion in the plasma membrane (McKenna *et al.*, 2019), to evaluate whether changes to cell wall integrity following ISX or Dri treatment might affect plasma membrane protein diffusion and complicate our interpretation of the PIP2A–GFP data. Short-term ISX treatment, as well as 5 d Dri treatment, reduced the recovery of LTI6B–GFP in the bleached region after 2 min (Supplementary Fig. S11), providing evidence that short-term ISX and constitutive Dri treatment reduces the mobility of LTI6B–GFP in the plasma membrane. Therefore, changes to lateral diffusion of plasma membrane-localized proteins are unlikely to have contributed to the increased recovery of PIP2A–GFP at the plasma membrane. Together, these results provide evidence that bulk secretion of proteins, and presumably cell wall material, is stimulated following short-term ISX or Dri treatment.

Cell wall integrity responses decrease endocytic trafficking

Given our results that cell wall modification by ISX or Dri increased anterograde trafficking, we next assessed the retrograde trafficking pathway by imaging the late endosome (LE) marker WAVE7–RFP, which labels RabF2a (Geldner *et al.*, 2009) (Fig. 4A; Supplementary Fig. S12A). Twenty-four hours

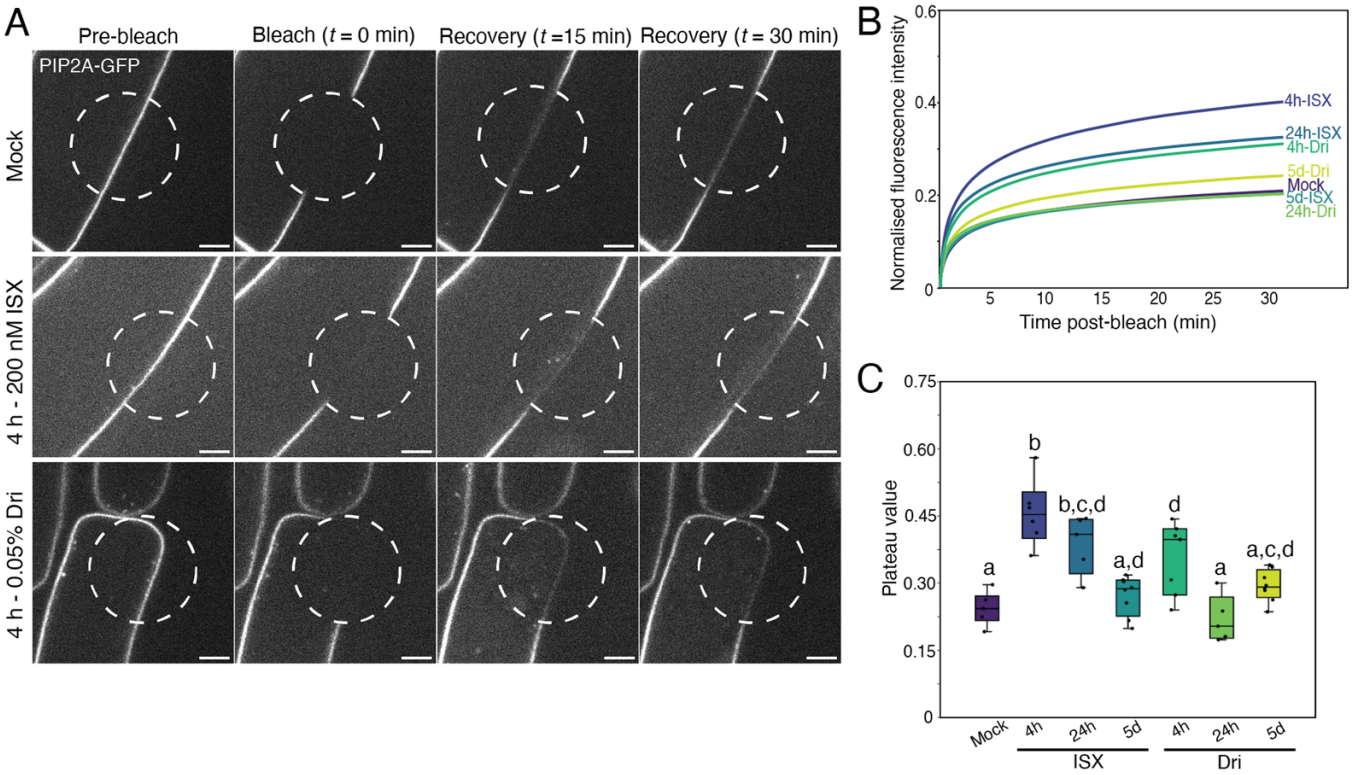

Fig. 3. PIP2A–GFP fluorescence recovery at the plasma membrane is increased with isoxaben (ISX) or Driselase (Dri). (A) Representative images of pre-bleach, bleach, and 15–30 min recovery of PIP2A–GFP fluorescence (white) in 5-day-old root elongation zone epidermal cells. The bleached region is outlined by a dashed white circle. Scale bars are 5 μm. (B) Mean fluorescence recovery curves of PIP2A–GFP following bleaching. (C) Plateau value, the fluorescence intensity at which the fluorescence recovery after photobleaching (FRAP) curve levels off, normalized to the pre-bleach value, following bleaching. n>5 regions of interest from five biological replicates. Letters indicate significantly different means using a one-way ANOVA with Dunn's post-hoc test with Bonferroni correction, P<0.05.

of ISX treatment increased LE size (Fig. 4B) but decreased the number of organelles (Fig. 4C), while there were no consistent trends for Dri treatment. No apparent changes were observed to LE ultrastructure using TEM images (Supplementary Fig. S8K–M), but this may be due to the earlier time point of high-pressure frozen seedlings for TEM (4 h) versus the later changes observed using fluorescence imaging (24 h). To monitor initial endocytosis from the plasma membrane, we quantified the uptake of the lipophilic dye FM1-43 (Emans *et al.*, 2002) following ISX or Dri treatment (Fig. 4D; Supplementary Fig. S12B). There were no significant differences for FM1-43 uptake within the first 5 min for any treatment, indicating that the initial steps of endocytosis are unaffected by these treatments (Supplementary Fig. S12C), but from 15–30 min there was a significant decrease in internal FM1-43 signal for 24 h and 5 d treatments of ISX or Dri (Supplementary Fig. S12D). After 60 min, FM1-43 uptake was significantly reduced in short-term ISX and 5 d Dri treatments (Fig. 4E). These results suggest that while the initial steps of endocytosis from the plasma membrane are unaffected following ISX or Dri treatment, the rate of endocytic trafficking from the early endosome to the late endosome and/or from the late endosome to the vacuole is reduced for short-term ISX and constitutive Dri treatments.

Disrupting cell wall integrity decreases organelle movement and dynamics of the actin cytoskeleton

During the live-cell imaging of the Golgi apparatus, TGN, and LE, we observed that organelle movement was reduced by ISX or Dri treatment. These results are similar to the reduced Golgi body movement following ISX treatment observed by Gutierrez *et al.* (2009). We quantified these using the Golgi marker NAG–GFP (Fig. 5; Supplementary Fig. S13A) and the LE marker WAVE7–RFP (Supplementary Fig. S13B, C). Both organelles showed significantly decreased speed following short-term ISX or 24 h Dri treatments. This effect was reversible, as 24 h ISX or Dri treatment followed by a 2 h washout in ½ MS medium significantly increased the movement of Golgi relative to 24 h-treated roots (Fig. 5B; Supplementary Fig. S13A).

Due to the association between organelle movement and the actin cytoskeleton (Nebenführ *et al.*, 1999), we hypothesized that the changes in organelle movement might be due to

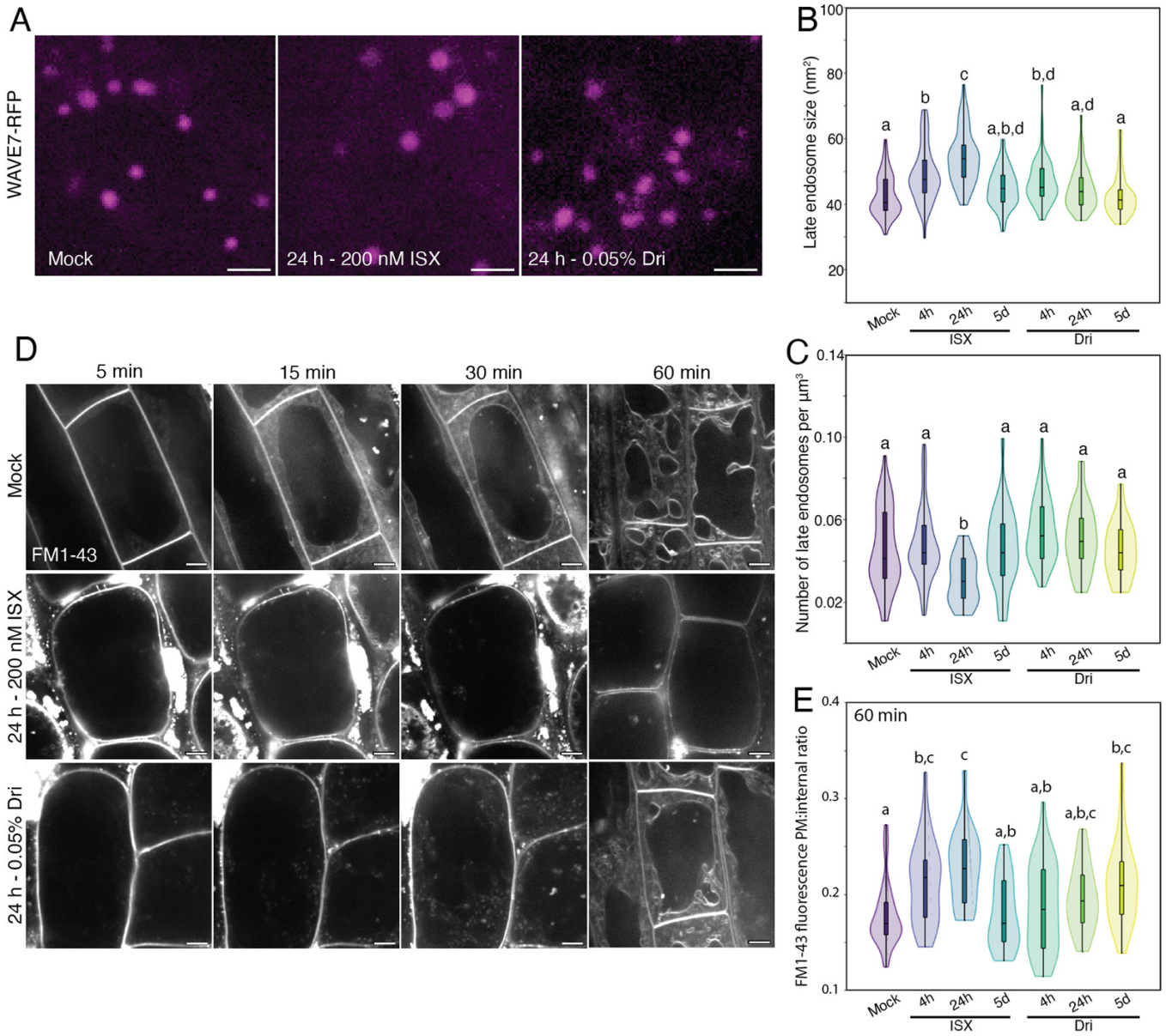

Fig. 4. Late endosome (LE) size is increased with isoxaben (ISX) treatment, and endocytic trafficking is reduced following ISX or Driselase (Dri) treatment. (A) Representative maximum-projection images of WAVE7–RFP LEs from 5-day-old, light-grown root elongation zone epidermal cells. (B) LE size. (C) LE number. *n*>45 regions of interest from 14 biological replicates. (D) Representative images of FM1-43 endocytosis in 5-day-old, light-grown root elongation zone epidermal cells after 5, 15, 30, or 60 min. Images from 5–30 min represent the same cell over a time progression, while images at 60 min represent different roots. (E) Quantification of plasma membrane (PM):internal ratio of FM1-43 after 60 min of endocytosis. *n*=17–24 cells from six biological replicates. Letters represent significantly different means using a one-way ANOVA and Dunn's post-hoc test with Bonferroni correction, $P<0.05$. Scale bars are 2 µm for (A) and 5 µm for (D).

changes to actin. We therefore imaged actin via fABD2–GFP, the fluorescently tagged f-actin binding domain of FIMBRIN1 (Sheahan *et al.*, 2004), following ISX or Dri treatment (Fig. 6A; Supplementary Fig. S14A). Actin occupancy (density, or a measure of local abundance) was significantly reduced in 24 h and 5 d treatments of ISX or Dri (Fig. 6B). Using a Pearson's correlation coefficient-based method to determine bulk actin remodelling and dynamics (Vidali *et al.*, 2010), we found that actin remodelling was significantly reduced by short-term treatment of ISX or Dri (Fig. 6C, D; Supplementary Fig. S14B). These results suggest that cell wall modification from ISX or Dri treatment impacts the organization and dynamics of the actin cytoskeleton, which may underlie the reduced organelle speeds that we observed.

To further connect the reduced actin dynamics with slower organelle movement, we treated seedlings with the

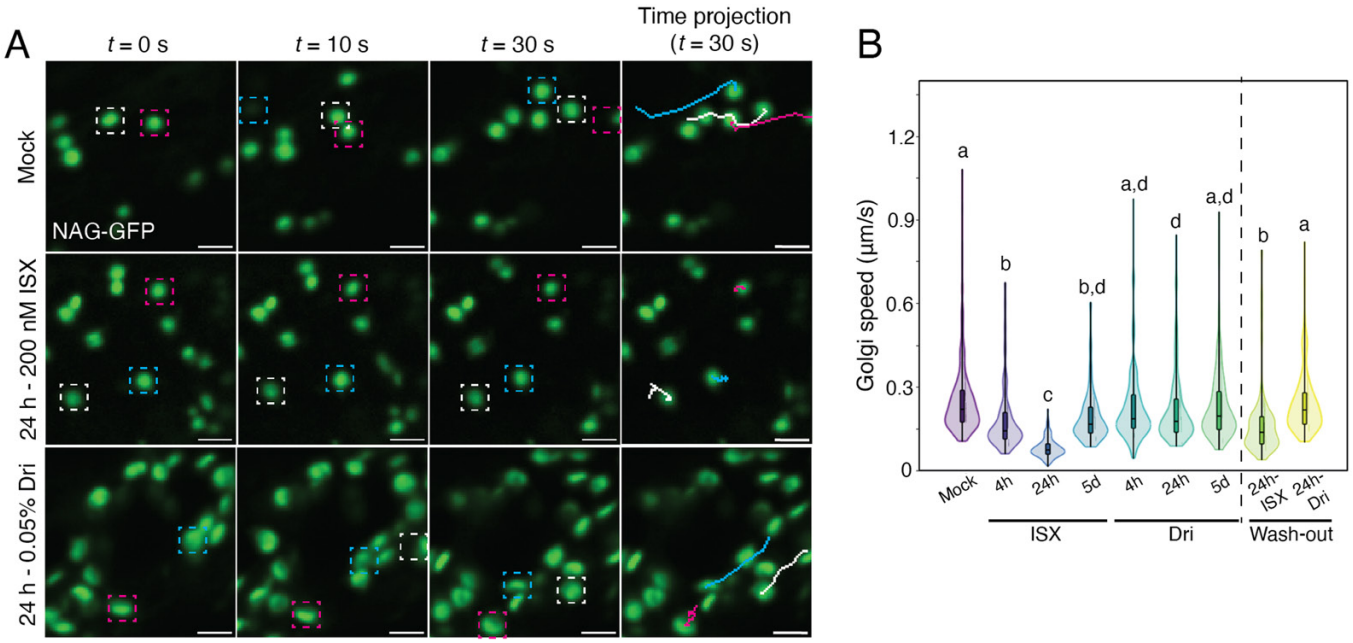

Fig. 5. Treatment with isoxaben (ISX) or Driselase (Dri) reduces Golgi speed. (A) Representative maximum-projection images from time lapses of Golgi (NAG–GFP; green) in 5-day-old Col-0 root elongation zone epidermal cells. Three representative Golgi bodies are tracked for 30 s and are indicated by white, magenta, or blue boxes. The final images show a line trace of the movement of the Golgi over 30 s. (B) Quantification of Golgi body speed. Wash-out experiments were performed by treating 5-day-old roots with 200 nM ISX or 0.05% Dri for 24 h, then moving them to normal ½ MS medium for 2 h prior to imaging. Scale bars are 2 µm. Letters represent significantly different values using a one-way ANOVA with Tukey's test, $P<0.01$. $n>78$ Golgi/treatment, from six biological replicates.

actin depolymerizing drug LatrunculinB (LatB; Baluška *et al.*, 2001). LatB treatment depolymerized the actin cytoskeleton as visualized by fABD2–GFP (Supplementary Fig. S15A) and significantly reduced Golgi body speed (Supplementary Fig. S15B, C). To test whether actin remodelling is important for the response to ISX or Dri, we co-treated seedlings with LatB and either ISX or Dri and measured root length after 4 h or 24 h treatment (Supplementary Fig. S15D). Co-treatment of ISX+LatB or Dri+LatB did not significantly impact root length at any time point relative to ISX or Dri treatment alone, indicating that actin remodelling is not strictly required following cell wall integrity disruption via ISX or Dri treatment.

Discussion

Changes to cell wall integrity triggered by isoxaben or Driselase treatment impact overlapping intracellular processes to increase secretion

In this work we provide evidence that cell wall modification broadly impacts cell morphology, endomembrane system structure and function, and organization and dynamics of the actin cytoskeleton (Fig. 7). We propose a model for how root cells respond to short-term cell wall modification following ISX or Dri treatment (Fig. 8). ISX treatment inhibits cellulose biosynthesis and activates cell wall signalling, perhaps through a mechanosensitive mechanism (Hamann *et al.*, 2009; Engelsdorf *et al.*, 2018). The weakening of the cell wall observed following ISX treatment (Bacete *et al.*, 2022) is caused by rapid internalization of CESAs from the plasma membrane (Paredez *et al.*, 2006) and consequently reduced cellulose production (Hamann *et al.*, 2009). The impact of ISX has been shown to be tissue-dependent and conditional on nutrient and sucrose concentration in the medium (Engelsdorf *et al.*, 2018; Ogden *et al.*, 2023). Dri weakens the cell wall via digestion of structural polysaccharides (Zhang *et al.*, 2019), presumably triggering mechanosensitive mechanisms and also causing release of small cell wall oligosaccharides from cellulose (Tseng *et al.*, 2022; Martín-Dacal *et al.*, 2023) or pectin (Voxeur *et al.*, 2019) that may bind to cognate receptors at the plasma membrane. Both treatments reduced actin dynamics, decreased organelle movement, and increased secretion while decreasing endocytic trafficking. Consistent with the altered trafficking pathways, organelle number and morphology were impacted, including increased LE size after ISX treatment, larger GA-TGN vesicles following Dri treatment, and larger Golgi bodies after both treatments. Interestingly, most of the changes observed under short-term modification were not seen in the constitutive treatments (Fig. 7), indicating that plant cells can habituate to low levels of cell wall signalling and/or cell wall stress over longer periods.

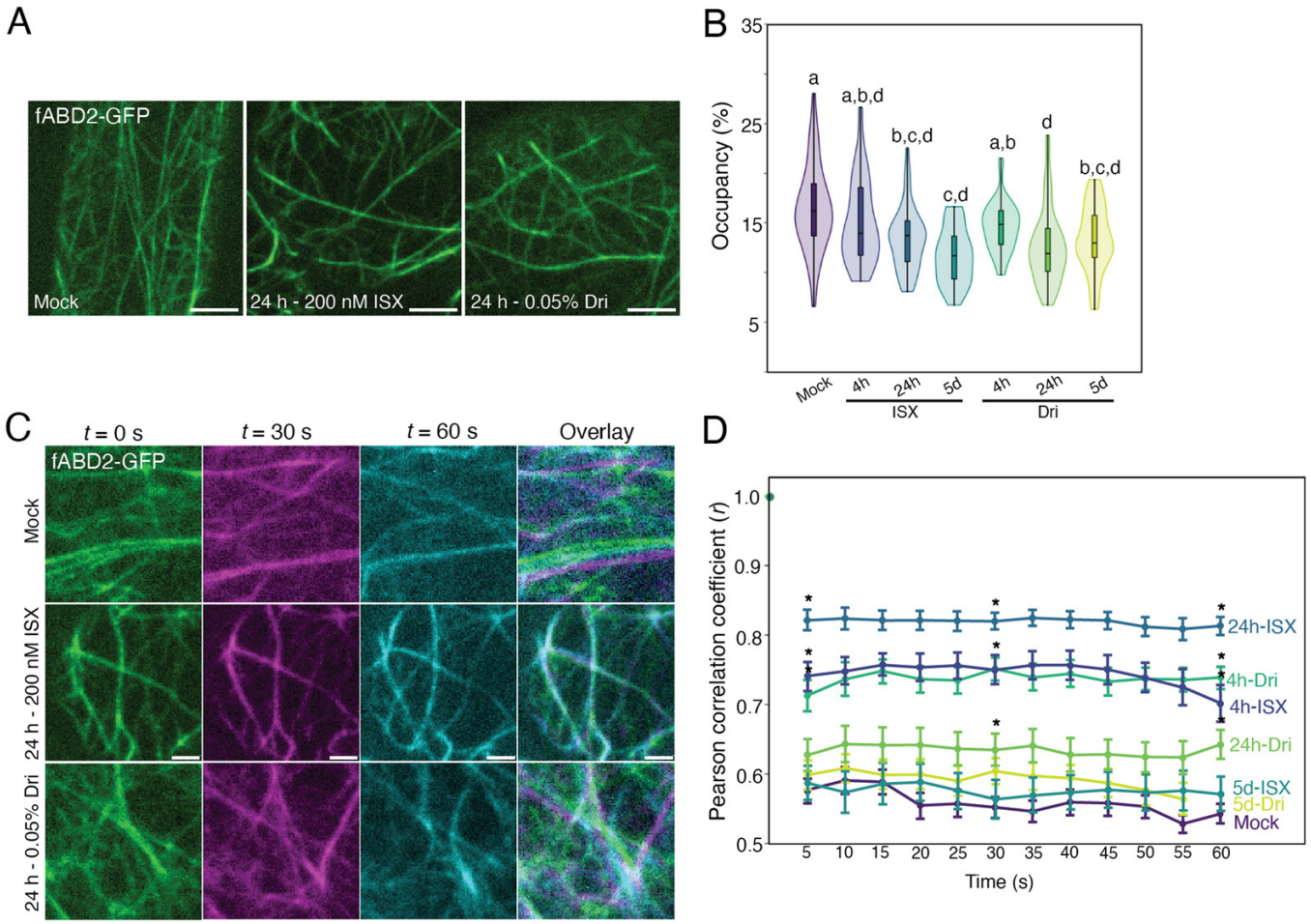

Fig. 6. Cortical actin occupancy and dynamics are decreased following isoxaben (ISX) or Driselase (Dri) treatment. (A) Representative maximum-projection images of 5-day-old fABD2–GFP root elongation zone epidermal cells. (B) Quantification of cortical actin occupancy (density). n>25 regions of interest for eight biological replicates. Letters represent significantly different means using a one-way ANOVA and Dunn's post-hoc test with Bonferroni correction, P<0.05. (C) Representative maximum-projection images of fABD2–GFP actin filaments at 0 s (green), 30 s (magenta), and 60 s (cyan), with overlaid image. The amount of overlap of the three colours indicates degree of actin dynamics over 60 s. (D) Pearson's correlation coefficient to quantify dynamics of actin over 60 s. A high Pearson's correlation coefficient indicates low dynamics (actin filaments do not change over time), whereas a low Pearson's correlation coefficient indicates increased dynamics. n=42 regions of interest from 14 biological replicates. Asterisks indicate significantly different means from Mock-treated seedlings at 5, 30, and 55 s using a one-way ANOVA and Dunn's post-hoc test with Bonferroni correction, P<0.05. Scale bars are 5 µm for (A) and 2 µm for (C).

Cell wall integrity responses impact organelle morphology and movement

We hypothesized that remodelling of intracellular processes, including production and secretion of new cell wall components, would occur between 4 and 24 h of cell wall modification. This was based on previous time course experiments in roots that indicated a transcriptional response after 3–4 h of ISX treatment (Hamann *et al.*, 2009), production of phytohormones by 7 h (Engelsdorf *et al.*, 2018), and altered cell wall composition by 12 h (Denness *et al.*, 2011). The precise time course following Dri treatment is less established, but severe root tip degradation and increased phytohormone levels were seen by 7 h and altered cell wall composition by 24 h (Engelsdorf *et al.*, 2018).

Golgi and TGN number, size, and ultrastructure have been shown to change in response to increased polysaccharide production (Young *et al.*, 2008; Wang *et al.*, 2017; Meents *et al.*, 2019) and stress conditions (Uemura *et al.*, 2019), so we first evaluated the ultrastructure of the Golgi apparatus and TGN. We hypothesized that GI-TGN number might be affected, specifically under Dri treatment, as cell wall damage and infection by powdery mildew increased the number of GI-TGNs (Uemura *et al.*, 2019). Unexpectedly, cell wall modification induced by ISX or Dri did not impact Golgi body or TGN number. Short-term ISX and Dri treatment increased Golgi body size, and Dri treatment specifically increased the size of GA-TGNs (Fig. 2), which is similar to the increased Golgi body and TGN size observed in cells undergoing higher rates

			ISX			Dri		
		Figure	4 h, 200 nM	24 h, 200 nM	5 d, 2 nM	4 h, 0.05%	24 h, 0.05%	5 d, 0.03%
Impact on plant development	Root length	Suppl. Figs S2–S5	−2	−38 *	−57 *	−10 *	−29 *	−39 *
Organelle morphology (confocal imaging)	Golgi size	Fig. 2B	1	26 *	8	22 *	25 *	5
	Number of Golgi	Fig. 2C	12	2	20	1	6	15
	TGN size	Fig. 2D	6	−8	25	4	2	11
	Number of GA-TGN	Suppl. Fig. S7E	17	9	14	−4	9	11
	Number of GI-TGN	Suppl. Fig. S7F	−9	−34	6	−34	−21	−22
	Proportion GI-TGN:GA-TGN	Fig. 2E	−3	−40 *	6	−29	−29	−27
	LE size	Fig. 4B	15 *	27 *	11	11 *	5	0
	Number of LEs	Fig. 4C	4	−33 *	2	20	12	−1
Organelle morphology (TEM imaging)	Golgi cisternae length	Suppl. Fig. S8E	−3	n.d.	n.d.	−3	n.d.	n.d.
	GA-TGN size	Fig. 2G	6	n.d.	n.d.	12 *	n.d.	n.d.
	GI-TGN size	Suppl. Fig. S8J	−2	n.d.	n.d.	−2	n.d.	n.d.
Secretion	Ratiometric-secGFP secretion	Suppl. Fig. S9	13 *	25 *	8 *	12 *	29 *	6
	PIP2A–GFP secretion (plateau)	Fig. 3C	88 *	59 *	12	46 *	−10	21
	LTI6B–GFP mobility (plateau)	Suppl. Fig. S11	−45 *	−60 *	−9	2	9	−35
Endocytic trafficking	FM1-43 uptake (60 minutes)	Fig. 4E	−14 *	−20 *	1	−2	−7	−14 *
Organelle and actin dynamics	Golgi speed	Fig. 5	−30 *	−69 *	−28 *	−14	−17 *	−12
	LE speed	Suppl. Fig. S13	−54 *	−64 *	−18	−16 *	−27 *	−24 *
	Actin occupancy (%)	Fig. 6B	−8	−19 *	−29 *	−11	−24 *	−19 *
	Actin dynamics	Fig. 6D	−27 *	−35 *	−9	−28 *	−15 *	−7

Fig. 7. Summary of spinning disk confocal and TEM imaging results from short-term and constitutive ISX and Dri treatment. The percentage change from Mock-treated seedlings is indicated, and the relative intensity of the change is visualized by a heatmap, where red indicates increased values relative to Mock-treated, white indicates no change from Mock-treated, and blue indicates decreased values relative to Mock-treated. Significant differences (P<0.05) from Mock-treated are denoted by asterisks. GA-TGN, Golgi-associated *trans*-Golgi network; GI-TGN, Golgi-independent *trans*-Golgi network; LE, late endosome; n.d., not determined; TEM, transmission electron microscopy.

of cell wall biosynthesis and secretion (Young *et al.*, 2008; Meents *et al.*, 2019). Despite observing no changes to TGN structure here, the TGN is important for ISX response, as mutants with defective TGN function were hypersensitive to ISX (Brüx *et al.*, 2008). Besides the changes to the Golgi apparatus and TGN, 24 h ISX treatment increased the size of LEs while decreasing the number of LEs.

Both biotic and abiotic stress can impact the rate of endocytosis or secretion. For example, increased secretion of cell wall components and defence compounds was observed following pathogen infection (Chowdhury *et al.*, 2014; Uemura *et al.*, 2019), and multiple studies have shown that osmotic (Zwiewka *et al.*, 2015) or salt (Luu *et al.*, 2012; Baral *et al.*, 2015) stresses can impact the rate of secretion or endocytosis.

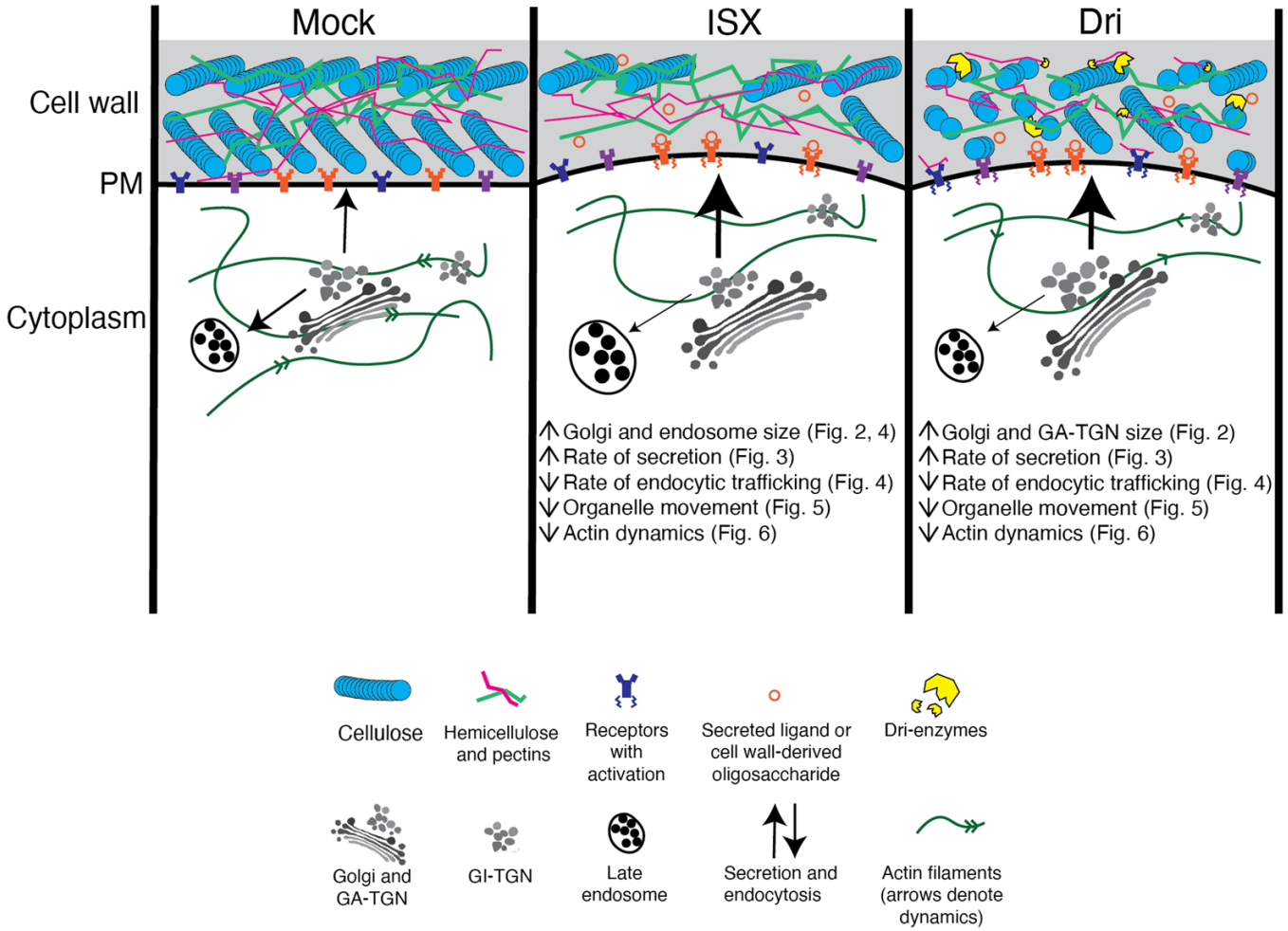

Fig. 8. Proposed model for how short-term cell wall integrity signalling triggered by isoxaben (ISX) or Driselase (Dri) impacts endomembrane system structure and function. Under ISX treatment, reduced cellulose synthesis presumably activates cell wall integrity signalling via receptors, which transduce intracellular signals. Golgi body and late endosome size is increased, while organelle movement significantly slows due to, in part, reduced actin dynamics. The rate of secretion increases, while the rate of endocytic trafficking decreases. Under Dri treatment, breakdown of cellulose and matrix polysaccharides activates cell wall integrity signalling. Golgi and GA-TGN size increases. Organelle movement and actin dynamics are decreased, and the rate of secretion is increased while rate of endocytic trafficking is decreased. GA-TGN, Golgi-associated *trans*-Golgi network; GI-TGN, Golgi-independent *trans*-Golgi network; PM, plasma membrane.

Furthermore, increased CESA enzyme secretion from the Golgi apparatus to the plasma membrane is required as part of cell wall fortification in response to cell wall integrity stresses, such as ISX treatment, and mutants with defects in this response are hypersensitive to ISX (McFarlane *et al.*, 2021; Vellosillo *et al.*, 2021). Altering the flux between anterograde or retrograde trafficking could modulate cell size and water content by adjusting the amount of membrane at the plasma membrane or changing the concentration of ion transporters or aquaporins (Zwiewka *et al.*, 2015). Following short-term treatment of ISX or Dri, we observed a significant increase in secretion of PIP2A–GFP to the plasma membrane (Fig. 3) and secreted GFP to the apoplast (Supplementary Fig. S9), suggesting that bulk secretion pathways were stimulated. Although we cannot exclude that increased PIP2A–GFP recovery could be due to changes to protein biosynthesis, the large increase in fluorescence recovery at the earliest time point following ISX or Dri treatment suggests it is not due to alterations in transcription or protein biosynthesis. There was also a significant decrease in the rate of FM1-43 endocytic trafficking (Fig. 4E) after 15–60 min. Increased secretory rates and decreased endocytic trafficking rates were also observed after 10 min in root cells during hypoosmotic stress (Zwiewka *et al.*, 2015), which causes cell swelling similar to ISX or Dri treatment, and there is a complex relationship between responses to changes to cell wall integrity and osmotic stress (Hamann *et al.*, 2009; Engelsdorf *et al.*, 2018). Therefore, it would be interesting to investigate the role of osmotic changes in cell wall responses in the future. Together, our results indicate that the balance between secretion and endocytic trafficking is adjusted when

cell wall integrity is perturbed, presumably to allow cell wall fortification.

Disrupting cell wall integrity may indirectly modify the actin cytoskeleton to compound impacts on intracellular trafficking and secretion

Previous studies have examined the effects of ISX on microtubule organization. Although ISX had no effect on *in vitro* microtubule polymerization (Fisher and Cyr, 1998), short-term ISX treatments, similar to our 4 h treatment, resulted in minor microtubule reorientation, from longitudinal to oblique orientation in root elongation zone cells (Paredez *et al.*, 2008). This reorientation may be the result of the mechanical equilibrium between cellulose synthesis and microtubule organization (Schneider *et al.*, 2022). Genetic disruption of cellulose synthesis did not affect microtubule orientation in the short term, but microtubule reorganization was observed after the onset of cell swelling, after 24 h (Sugimoto *et al.*, 2001). The effect of Dri treatment on microtubules has not been examined, but microtubules are sensitive to physical signals from the cell wall (Hardham *et al.*, 2008), which may be impacted by cell wall digestion through Dri. During the live-cell imaging, we observed that organelle movement and actin dynamics were significantly reduced following short-term treatments of ISX or Dri, with organelles being almost immobile following 24 h ISX treatment, but that this movement significantly recovered after 2 h wash-out (Fig. 5). This is similar to the decreased actin dynamics seen in mature rosette cells following ISX treatment (Tolmie *et al.*, 2017). An altered actin cytoskeleton has also been shown to decrease the rate of endocytosis of the dye FM4-64 (Sampathkumar *et al.*, 2013), which could also explain the reduced endocytic trafficking observed in this study following short-term ISX or Dri treatment. However, actin remodelling was not strictly required for plant growth responses under ISX or Dri treatment (Supplementary Fig. S14).

While this study has informed on the various intracellular changes that occur at different time points following cell wall modification, the underlying mechanisms for how these processes happen are still unknown. Changes to the morphology and function of the endomembrane system following cell wall modification could be mediated through direct and indirect mechanisms. For example, the small GTPases ROP1 and ROP6 are implicated in actin cytoskeleton regulation and trafficking of endomembrane vesicles (Chen *et al.*, 2012; Venus and Oelmüller, 2013). Recent work has shown that the cell wall integrity sensor FERONIA (FER) is upstream of ROP6 activity following mechanosensing (Tang *et al.*, 2022), changes to pectin methylesterification status (Lin *et al.*, 2022), or osmotic stress (Smokvarska *et al.*, 2023). Therefore, future work could examine whether the reduced dynamics of the actin cytoskeleton following ISX or Dri treatment is FER- and/or ROP6-dependent.

Together, the results from this work indicate that activation of cell wall integrity responses impacts cell morphology, plasma membrane dynamics, structure and function of the endomembrane system, and organization and movement of the actin cytoskeleton. These internal changes could provide mechanisms to produce new cell wall components to fortify the cell wall and protect the cell from bursting when cell wall integrity is compromised.

Supplementary data

The following supplementary data are available at *JXB* online.

Fig. S1. Summary of previous research examining short-term impact of ISX on Arabidopsis seedlings.

Fig. S2. Constitutive growth on ISX reduces root and hypocotyl growth and impacts tissue morphology.

Fig. S3. Short-term treatment of 200 nM ISX impacts growth and cell morphology.

Fig. S4. Constitutive growth on Dri reduces growth and alters tissue morphology in light-grown roots.

Fig. S5. Short-term treatment of 0.05% Dri impacts plant growth and cell morphology.

Fig. S6. ISX and Dri cause cell swelling, but heat-inactivated Dri has only minor effects.

Fig. S7. Other time points and parameters examining impact of ISX or Dri on the Golgi and TGN.

Fig. S8. Additional TEM images and quantification.

Fig. S9. ISX and Dri treatment impact secretion to the apoplast.

Fig. S10. Additional data for PIP2A–GFP FRAP.

Fig. S11. LTI6B–GFP FRAP following ISX or Dri treatment.

Fig. S12. Additional time points for LE size and number, and endocytic trafficking of FM1-43.

Fig. S13. Additional time points for movement of Golgi and measurements of LE speed following ISX or Dri treatment.

Fig. S14. Additional images for cortical actin organization and dynamics following ISX or Dri treatment.

Fig. S15. LatB depolymerizes actin filaments, reduces Golgi speed, and impacts plant growth, but does not exacerbate cell wall integrity signalling-induced phenotypes.

Table S1. Fluorescent lines used for imaging.

Acknowledgements

We would like to thank the CSB Imaging Facility and the SickKids Nanoscale Biomedical Imaging Facility for their technical support and advice.

Author contributions

NH and HEM were involved in project conceptualization. NH, EM, and HEM performed the formal analyses. NH generated the methodology and performed the data visualization. NH wrote the original draft of the

manuscript, and NH, EM, and HEM contributed to reviewing and editing. HEM was involved in funding acquisition and supervision.

Conflict of interest

The authors declare they have no conflict of interest.

Funding

HEM is the Canada Research Chair in Plant Cell Biology. This work was supported by the Natural Sciences and Engineering Research Council of Canada NSERC Discovery Grant (2020-05959), Canada Foundation for Innovation and the Ontario Research Fund grants (38721), and an Ontario Early Researcher Award (ER21-16-256) to HEM, an NSERC Canada Doctoral Scholarship and an Ontario Graduate Scholarship to NH.

Data availability

The data underlying this article will be shared upon request to the corresponding author.

References

Anderson CT, Kieber JJ. 2020. Dynamic construction, perception, and remodeling of plant cell walls. Annual Review of Plant Biology **71**, 39–69.

Bacete L, Hamann T. 2020. The role of mechanoperception in plant cell wall integrity maintenance. Plants **9**, 574.

Bacete L, Schulz J, Engelsdorf T, *et al*. 2022. THESEUS1 modulates cell wall stiffness and abscisic acid production in *Arabidopsis thaliana*. Proceedings of the National Academy of Sciences, USA **119**, e2119258119.

Baluška F, Jasik J, Edelmann HG, Salajová T, Volkmann D. 2001. Latrunculin B-induced plant dwarfism: plant cell elongation is F-actin-dependent. Developmental Biology **231**, 113–124.

Baral A, Irani NG, Fujimoto M, Nakano A, Mayor S, Mathew MK. 2015. Salt-induced remodeling of spatially restricted clathrin-independent endocytic pathways in Arabidopsis root. The Plant Cell **27**, 1297–1315.

Bolte S, Cordelières FP. 2006. A guided tour into subcellular colocalization analysis in light microscopy. Journal of Microscopy **224**, 213–232.

Brüx A, Liu TY, Krebs M, Stierhof YD, Lohmann JU, Miersch O, Wasternack C, Schumacher K. 2008. Reduced V-ATPase activity in the *trans*-Golgi network causes oxylipin-dependent hypocotyl growth inhibition in *Arabidopsis*. The Plant Cell **20**, 1088–1100.

Chaudhary A, Chen X, Gao J, Leśniewska B, Hammerl R, Dawid C, Schneitz K. 2020. The *Arabidopsis* receptor kinase STRUBBELIG regulates the response to cellulose deficiency. PLoS Genetics **16**, e1008433.

Chen X, Naramoto S, Robert S, Tejos R, Löfke C, Lin D, Yang Z, Friml J. 2012. ABP1 and ROP6 GTPase signaling regulate clathrin-mediated endocytosis in *Arabidopsis* roots. Current Biology **22**, 1326–1332.

Chowdhury J, Henderson M, Schweizer P, Burton RA, Fincher GB, Little A. 2014. Differential accumulation of callose, arabinoxylan and cellulose in nonpenetrated versus penetrated papillae on leaves of barley infected with *Blumeria graminis* f. sp. *hordei*. New Phytologist **204**, 650–660.

Crowell EF, Bischoff V, Desprez T, Rolland A, Stierhof YD, Schumacher K, Gonneau M, Höfte H, Vernhettes S. 2009. Pausing of Golgi bodies on microtubles regulates secretion of cellulose synthase complexes in *Arabidopsis*. The Plant Cell **21**, 1141–1154.

Cutler SR, Ehrhardt DW, Griffitts JS, Somerville CR. 2000. Random GFP::cDNA fusions enable visualization of subcellular structures in cells of *Arabidopsis* at a high frequency. Proceedings of the National Academy of Sciences, USA **97**, 3718–3723.

Denness L, McKenna JF, Segonzac C, Wormit A, Madhou P, Bennett M, Mansfield J, Zipfel C, Hamann T. 2011. Cell wall damage-induced lignin biosynthesis is regulated by a reactive oxygen species- and jasmonic acid-dependent process in Arabidopsis. Plant Physiology **156**, 1364–1374.

Desprez T, Juraniec M, Crowell EF, Jouy H, Pochylova Z, Parcy F, Höfte H, Gonneau M, Vernhettes S. 2007. Organization of cellulose synthase complexes involved in primary cell wall synthesis in *Arabidopsis thaliana*. Proceedings of the National Academy of Sciences, USA **104**, 15572–15577.

Dettmer J, Hong-Hermesdorf A, Stierhof YD, Schumacher K. 2006. Vacuolar H^+-ATPase activity is required for endocytic and secretory trafficking in *Arabidopsis*. The Plant Cell **18**, 715–730.

Duval I, Beaudoin N. 2009. Transcriptional profiling in response to inhibition of cellulose synthesis by thaxtomin A and isoxaben in *Arabidopsis thaliana* suspension cells. Plant Cell Reports **28**, 811–830.

Emans N, Zimmermann S, Fischer R. 2002. Uptake of a fluorescent marker in plant cells is sensitive to Brefeldin A and wortmannin. The Plant Cell **14**, 71–86.

Engelsdorf T, Gigli-Bisceglia N, Veerabagu M, McKenna JF, Vaahtera L, Augstein F, Van der Does D, Zipfel C, Hamann T. 2018. The plant cell wall integrity maintenance and immune signaling systems cooperate to control stress responses in *Arabidopsis thaliana*. Science Signaling **11**, 536.

Feraru E, Feraru MI, Kleine-Vehn J, Martinière A, Mouille G, Vanneste S, Vernhettes S, Runions J, Friml J. 2011. PIN polarity maintenance by the cell wall in *Arabidopsis*. Current Biology **21**, 338–343.

Fisher DD, Cyr RJ. 1998. Extending the microtubule/microfibril paradigm: Cellulose synthesis is required for normal cortical microtubule aligment in elongating cells. Plant Physiology **116**, 1043–1051.

Geldner N, Dénervaud-Tendon V, Hyman DL, Mayer U, Stierhof YD, Chory J. 2009. Rapid, combinatorial analysis of membrane compartments in intact plants with a multicolor marker set. The Plant Journal **59**, 169–178.

Gigli-Bisceglia N, Engelsdorf T, Strnad M, *et al.* 2018. Cell wall integrity modulates *Arabidopsis thaliana* cell cycle gene expression in a cytokinin- and nitrate reductase-dependent manner. Development **145**, dev166678.

Gilles JF, Dos Santos M, Boudier T, Bolte S, Heck N. 2017. DiAna, an ImageJ tool for object-based 3D co-localization and distance analysis. Methods **115**, 55–64.

Grebe M, Xu J, Möbius W, Ueda T, Nakano A, Geuze HJ, Rook MB, Scheres B. 2003. *Arabidopsis* sterol endocytosis involves actin-mediated trafficking via ARA6-positive early endosomes. Current Biology **13**, 1378–1387.

Gutierrez R, Lindeboom JJ, Paredez AR, Emons AMC, Ehrhardt DW. 2009. *Arabidopsis* cortical microtubules position cellulose synthase delivery to the plasma membrane and interact with cellulose synthase trafficking compartments. Nature Cell Biology **11**, 797–806.

Hamann T, Bennett M, Mansfield J, Somerville C. 2009. Identification of cell-wall stress as a hexose-dependent and osmosensitive regulator of plant responses. The Plant Journal **57**, 1015–1026.

Hardham AR, Takemoto D, White RG. 2008. Rapid and dynamic subcellular reorganization following mechanical stimulation of *Arabidopsis* epidermal cells mimics responses to fungal and oomycete attack. BMC Plant Biology **8**, 63.

Heinze L, Freimuth N, Rößling A-K, Hahnke R, Riebschläger S, Fröhlich A, Sampathkumar A, McFarlane HE, Sauer M. 2020. EPSIN1 and MTV1 define functionally overlapping but molecularly distinct *trans*-Golgi network subdomains in *Arabidopsis*. Proceedings of the National Academy of Sciences, USA **117**, 25880–25889.

Higaki T. 2017. Quantitative evaluation of cytoskeletal organizations by microscopic image analysis. Plant Morphology **29**, 15–21.

Hoffmann N, King S, Samuels AL, McFarlane HE. 2021. Subcellular coordination of plant cell wall synthesis. Developmental Cell **56**, 933–948.

Kang BH, Nielsen E, Preuss ML, Mastronarde D, Staehelin LA. 2011. Electron tomography of RabA4b- and PI-4Kβ1-labeled *trans* Golgi network compartments in *Arabidopsis*. Traffic **12**, 313–329.

Kesten C, Gámez-Arjona FM, Menna A, *et al*. 2019. Pathogen-induced pH changes regulate the growth-defense balance in plants. The EMBO Journal **38**, e101822.

Kubicek CP, Starr TL, Glass NL. 2014. Plant cell wall-degrading enzymes and their secretion in plant-pathogenic fungi. Annual Review of Phytopathology **52**, 427–451.

Lin W, Tang W, Pan X, Huang A, Gao X, Anderson CT, Yang Z. 2022. *Arabidopsis* pavement cell morphogenesis requires FERONIA binding to pectin for activation of ROP GTPase signaling. Current Biology **32**, 497–507.e4.

Luu DT, Martiniãre A, Sorieul M, Runions J, Maurel C. 2012. Fluorescence recovery after photobleaching reveals high cycling dynamics of plasma membrane aquaporins in Arabidopsis roots under salt stress. The Plant Journal **69**, 894–905.

Martín-Dacal M, Fernández-Calvo P, Jiménez-Sandoval P, *et al*. 2023. Arabidopsis immune responses triggered by cellulose- and mixed-linkage glucan-derived oligosaccharides require a group of leucine-rich repeat malectin receptor kinases. The Plant Journal **113**, 833–850.

Martinière A, Lavagi I, Nageswaran G, *et al*. 2012. Cell wall constrains lateral diffusion of plant plasma-membrane proteins. Proceedings of the National Academy of Sciences, USA **109**, 12805–12810.

McFarlane HE, Mutwil-Anderwald J, Verbančič J, *et al*. 2021. A G protein-coupled receptor-like module regulates cellulose synthase secretion from the endomembrane system in Arabidopsis. Developmental Cell **56**, 1484–1497.

McKenna JF. 2022. Quantifying the organization and dynamics of the plant plasma membrane across scales using light microscopy. In: Benitez-Alfonso Y, Heinlein M, eds. Methods in Molecular Biology, vol 2457. New York: Humana, 233–251.

McKenna JF, Rolfe DJ, Webb SED, Tolmie AF, Botchway SW, Martin-Fernandez ML, Hawes C, Runions J. 2019. The cell wall regulates dynamics and size of plasma-membrane nanodomains in *Arabidopsis*. Proceedings of the National Academy of Sciences, USA **116**, 12857–12862.

Meents MJ, Motani S, Mansfield SD, Samuels AL. 2019. Organization of xylan production in the Golgi during secondary cell wall biosynthesis. Plant Physiology **181**, 527–546.

Nebenführ A, Gallagher LA, Dunahay TG, Frohlick JA, Mazurkiewicz AM, Meehl JB, Staehelin LA. 1999. Stop-and-go movements of plant Golgi stacks are mediated by the acto-myosin system. Plant Physiology **121**, 1127–1142.

Oda Y, Asatsuma S, Nakasone H, Matsuoka K. 2020. Sucrose starvation induces the degradation of proteins in *trans*-Golgi network and secretory vesicle cluster in tobacco BY-2 cells. Bioscience, Biotechnology and Biochemistry **84**, 1652–1666.

Ogden M, Whitcomb SJ, Khan GA, Roessner U, Hoefgen R, Persson S. 2023. Cellulose biosynthesis inhibitor isoxaben causes nutrient-dependent and tissue-specific Arabidopsis phenotypes. Plant Physiology **194**, 612–617.

Paredez AR, Persson S, Ehrhardt DW, Somerville CR. 2008. Genetic evidence that cellulose synthase activity influences microtubule cortical array organization. Plant Physiology **147**, 1723–1734.

Paredez AR, Somerville C, Ehrhardt D. 2006. Visualization of cellulose synthase demonstrates functional association with microtubules. Science **312**, 1491–1495.

Pedersen GB, Blaschek L, Frandsen KEH, Noack LC, Persson S. 2023. Cellulose synthesis in land plants. Molecular Plant **16**, 206–231.

Reynolds ES. 1963. The use of lead citrate at high pH as an electron-opaque stain in electron microscopy. The Journal of Cell Biology **17**, 208–212.

Samalova M, Fricker M, Moore I. 2006. Ratiometric fluorescence-imaging assays of plant membrane traffic using polyproteins. Traffic **7**, 1701–1723.

Sampathkumar A, Gutierrez R, McFarlane HE, Bringmann M, Lindeboom J, Emons A-M, Samuels L, Ketelaar T, Ehrhardt DW, Persson S. 2013. Patterning and lifetime of plasma membrane-localized cellulose synthase is dependent on actin organization in Arabidopsis interphase cells. Plant Physiology **162**, 675–688.

Scheible WR, Eshed R, Richmond T, Delmer D, Somerville C. 2001. Modifications of cellulose synthase confer resistance to isoxaben and thiazolidinone herbicides in *Arabidopsis ixr1* mutants. Proceedings of the National Academy of Sciences, USA **98**, 10079–10084.

Schindelin J, Arganda-Carreras I, Frise E, *et al*. 2012. Fiji: an open-source platform for biological-image analysis. Nature Methods **9**, 676–682.

Schneider R, Ehrhardt DW, Meyerowitz EM, Sampathkumar A. 2022. Tethering of cellulose synthase to microtubules dampens mechano-induced cytoskeletal organization in *Arabidopsis* pavement cells. Nature Plants **8**, 1064–1073.

Sheahan MB, Staiger CJ, Rose RJ, McCurdy DW. 2004. A green fluorescent protein fusion to actin-binding domain2 of Arabidopsis fimbrin highlights new features of a dynamic actin cytoskeleton in live plant cells. Plant Physiology **136**, 3968–3978.

Shimizu Y, Takagi J, Ito E, *et al*. 2021. Cargo sorting zones in the *trans*-Golgi network visualized by super-resolution confocal live imaging microscopy in plants. Nature Communications **12**, 1901.

Smokvarska M, Bayle V, Maneta-Peyret L, *et al*. 2023. The receptor kinase FERONIA regulates phosphatidylserine localization at the cell surface to modulate ROP signaling. Science Advances **9**, 14.

Sugimoto K, Williamson RE, Wasteneys GO. 2001. Wall architecture in the cellulose-deficient *rsw1* mutant of *Arabidopsis thaliana*: Microfibrils but not microtubules lose their transverse alignment before microfibrils become unrecognizable in the mitotic and elongation zone of roots. Protoplasma **215**, 172–183.

Tang W, Lin W, Zhou X, Guo J, Dang X, Li B, Deshu L, Yang Z. 2022. Mechano-transduction via the pectin-FERONIA complex activates ROP6 GTPase signaling in *Arabidopsis* pavement cell morphogenesis. Current Biology **32**, 508–517.

Tolmie F, Poulet A, McKenna J, Sassmann S, Graumann K, Deeks M, Runions J. 2017. The cell wall of *Arabidopsis thaliana* influences actin network dynamics. Journal of Experimental Botany **68**, 4517–4527.

Tseng Y-H, Scholz SS, Fliegmann J, Krüger T, Gandhi A, Furch ACU, Kniemeyer O, Brakhage AA, Oelmüller R. 2022. CORK1, A LRR-malectin receptor kinase, is required for cellooligomer-induced responses in *Arabidopsis thaliana*. Cells **11**, 2960.

Uemura T, Nakano RT, Takagi J, *et al*. 2019. A Golgi-released subpopulation of the *trans*-Golgi network mediates protein secretion in Arabidopsis. Plant Physiology **179**, 519–532.

Uemura T, Suda Y, Ueda T, Nakano A. 2014. Dynamic behavior of the *trans*-Golgi network in root tissues of Arabidopsis revealed by super-resolution live imaging. Plant and Cell Physiology **55**, 694–703.

Vaahtera L, Schulz J, Hamann T. 2019. Cell wall integrity maintenance during plant development and interaction with the environment. Nature Plants **5**, 924–932.

Vellosillo T, Dinneny JR, Somerville CR, Ehrhardt DW. 2021. TRANVIA (TVA) facilitates cellulose synthase trafficking and delivery to the plasma membrane. Proceedings of the National Academy of Sciences, USA **118**, e2021790118.

Venus Y, Oelmüller R. 2013. Arabidopsis ROP1 and ROP6 influence germination time, root morphology, the formation of F-actin bundles, and symbiotic fungal interactions. Molecular Plant **6**, 872–886.

Verbančič J, Huang J, McFarlane HE. 2021. Analysis of cellulose synthase activity in Arabidopsis using spinning disk microscopy. STAR Protocols **2**, 100863.

Vidali L, Burkart GM, Augustine RC, Kerdavid E, Tüzel E, Bezanilla M. 2010. Myosin XI is essential for tip growth in *Physcomitrella patens*. The Plant Cell **22**, 1868–1882.

Viotti C, Bubeck J, Stierhof Y-D, *et al*. 2010. Endocytic and secretory traffic in *Arabidopsis* merge in the *trans*-Golgi network/early endosome, an independent and highly dynamic organelle. The Plant Cell **22**, 1344–1357.

Voxeur A, Habrylo O, Guénin S, *et al*. 2019. Oligogalacturonide production upon *Arabidopsis thaliana-Botrytis cinerea* interaction. Proceedings of the National Academy of Sciences, USA **116**, 19743–19752.

Wang P, Chen X, Goldbeck C, Chung E, Kang BH. 2017. A distinct class of vesicles derived from the *trans*-Golgi mediates secretion of xylogalacturonan in the root border cell. The Plant Journal **92**, 596–610.

Wang P, Hsu CC, Du Y, *et al*. 2020. Mapping proteome-wide targets of protein kinases in plant stress responses. Proceedings of the National Academy of Sciences, USA **117**, 3270–3280.

Wormit A, Butt SM, Chairam I, *et al*. 2012. Osmosensitive changes of carbohydrate metabolism in response to cellulose biosynthesis inhibition. Plant Physiology **159**, 105–117.

Young RE, McFarlane HE, Hahn MG, Western TL, Haughn G, Samuels AL. 2008. Analysis of the Golgi apparatus in *Arabidopsis* seed coat cells during polarized secretion of pectin-rich mucilage. The Plant Cell **20**, 1623–1638.

Zhang T, Tang H, Vavylonis D, Cosgrove DJ. 2019. Disentangling loosening from softening: insights into primary cell wall structure. The Plant Journal **100**, 1101–1117.

Zhu Y, McFarlane HE. 2022. Regulation of cellulose synthesis via exocytosis and endocytosis. Current Opinion in Plant Biology **69**, 102273.

Zwiewka M, Nodzyński T, Robert S, Vanneste S, Friml J. 2015. Osmotic stress modulates the balance between exocytosis and clathrin-mediated endocytosis in *Arabidopsis thaliana*. Molecular Plant **8**, 1175–1187.